TURBULENCE ANISOTROPY IN A BUBBLY VERTICAL CHANNEL FLOW WITH TOPOLOGICAL CHANGES

Arturo A. Arosemena
Department of Chemical Engineering
Norwegian University of Science and Technology
Sem Sælands vei 6, Trondheim, Trøndelag, 7491, Norway
arturo.arosemena@ntnu.no

Davide Procacci
FLOW, Department of Engineering Mechanics
KTH Royal Institute of Technology
Osquars backe 18, Stockholm, Stockholms län, 114 28, Sweden
procacci@kth.se

Simone Di Giorgio
Istituto di Ingegneria del Mare
Consiglio Nazionale delle Ricerche
Via di Vallerano 139, Rome, Lazio, 00128, Italy
simone.digiorgio@cnr.it

Jannike Solsvik
Department of Chemical Engineering
Norwegian University of Science and Technology
Sem Sælands vei 6, Trondheim, Trøndelag, 7491, Norway
jannike.solsvik@ntnu.no

Shahab Mirjalili
FLOW, Department of Engineering Mechanics
KTH Royal Institute of Technology
Osquars backe 18, Stockholm, Stockholms län, 114 28, Sweden
msey@kth.se

ABSTRACT

High-fidelity numerical simulations of bubble-laden, vertical channel flow in the upward configuration, where the bubbles undergo topological changes (breakup and coalescence), were performed with the purpose of exploring the effect of the surface tension on the turbulence anisotropy in the carrier phase. A qualitative analysis shows that velocity fluctuations are enhanced in the wake of large bubbles. Moreover, as shown by the velocity spectra, these structures seem to scale with bubble size and interact with those closer to the wall. Finally, a barycentric map and other indicators of turbulence anisotropy clarify that, except at the core of the channel where the largest bubbles reside, the multiphase flow cases are actually more isotropic than the single-phase flow at a matching friction Reynolds number. This unexpected behavior is attributed to a better redistribution of energy due to an enhancement of sweep events (high-speed fluid towards the wall) in the presence of large bubbles.

INTRODUCTION

Turbulent bubbly flows are found in a multitude of settings. From wave breaking on the surface of oceans to bubble column reactors and piping systems used in industrial applications. In many instances, these flows present two-way coupled dynamics between the phases, making their analysis quite complex. In particular, in the case of bubbly flow delimited by walls, velocity fluctuations in the carrier may arise not only due to the action of an external pressure gradient or imposed flow rate–as in single-phase flow–but also due to buoyancy and the generation of bubble-induced agitation (Risso, 2018). In addition, other effects such as interface contamination, gas volume fraction, bubble deformability, and topological changes in the dispersed phase (i.e., breakage and coalescence) may affect the bubbly flow motion.

Regarding the study of turbulent bubbly flow that undergoes topological changes, there is in fact a gap in the literature. Many experiments and nearly all numerical simulations have focused on dispersed flow where bubbles, for the most part, do not go through changes in topology (Garbin *et al.*, 2025). It was not until fairly recently that works on the statistical description of turbulent bubbly flows with bubbles undergoing breakup and coalescence started to be reported (Lu & Tryggvason, 2018, 2019; Lu *et al.*, 2025). Furthermore, the focus of these studies has been the investigation of low-order statistics (e.g., mean values, variances, and covariance) with little attention to proper characterization of the states of turbulence; information that is key for the validation and advancement of second-moment closures for the modeling of turbulent bubbly flow (Ma *et al.*, 2020). In this context, Procacci *et al.* (2026) recently conducted the first investigation on turbulence anisotropy in heterogeneous bubbly flow with topological changes. Here, we expand the qualitative discussion, including velocity spectra, and provide a summary of the key findings.

NUMERICAL SIMULATIONS

High-fidelity numerical simulations of a three-dimensional, bubble-laden vertical channel in the up-flow configuration were performed. See figure 1. The computation domain has a size of $4\pi h \times 2h \times 2\pi h$ in the x (streamwise), y (wall-normal) and z (spanwise) directions, respectively. Note that, h (half-channel width) is the characteristic length and u_τ (friction velocity) is the characteristic velocity scale. The flow is driven by an effective constant pressure gradient that also accounts for the weight of the mixture. Periodicity is imposed for all variables in x and z, while the no-slip and impermeability boundary conditions are imposed for the velocity field at the walls. A right constant angle ($\pi/2$) is imposed for the phase indicator. The code solves the one-fluid incompressible Navier–Stokes equations and the interface is captured using a volume-of-fluid (VOF) method (Weymouth & Yue, 2010). Details about the numerical implementation and a thorough validation of the code are found in Di Giorgio *et al.* (2024) and Rossi *et al.* (2025), respectively.

In this problem, the important physical parameters are Re_τ (friction Reynolds number; ratio of inertial to viscous forces), We_τ (friction Weber number; ratio of inertial to surface tension forces) and Fr (Froude number; ratio of inertial to buoyancy forces). In addition, the multiphase flow is also characterized by α (gas volume fraction), ρ_r (density ratio; bubbles to carrier phase), and μ_r (dynamic viscosity ratio; bubbles to carrier phase). With the objective of studying turbulence anisotropy with surface tension–thus, for cases with differences in the breakage and coalescence events–multiphase simulations with three different We_τ were carried out: 2.8, 1.4, and 0.7. All other parameters were kept constant: $Re_\tau = 150$, $Fr = 0.014$, $\alpha = 5.4\%$, $\rho_r = 0.1$, and $\mu_r = 1$. The results of a single-phase (SP) simulation at $Re_\tau = 150$ serve as a basis for comparison with the multiphase cases.

It is also noted that a fixed grid resolution was used in all simulations. For the two homogeneous directions, a constant grid spacing of $\Delta x^+ = \Delta z^+ = 1.84$ was considered. On the other hand, in the wall-normal direction, a natural grid stretching was employed (Pirozzoli & Orlandi, 2021), with a minimum resolution near the wall of $\Delta y^+_{min} = 0.041$ and a maximum resolution at the channel center of $\Delta y^+_{max} = 1.76$. Here, the superscript $+$ is used to denote viscous units. In the following, to facilitate comparison with SP and homogeneous bubbly channel flow, we only show information corresponding to the largest and smallest We_τ cases, that is, 2.8 and 0.7. For a more complete report of the different cases and for further details about the simulations performed, see Procacci *et al.* (2026).

RESULTS

Before discussing the states of turbulence in the carrier, we consider some relevant qualitative features of the multiphase flow.

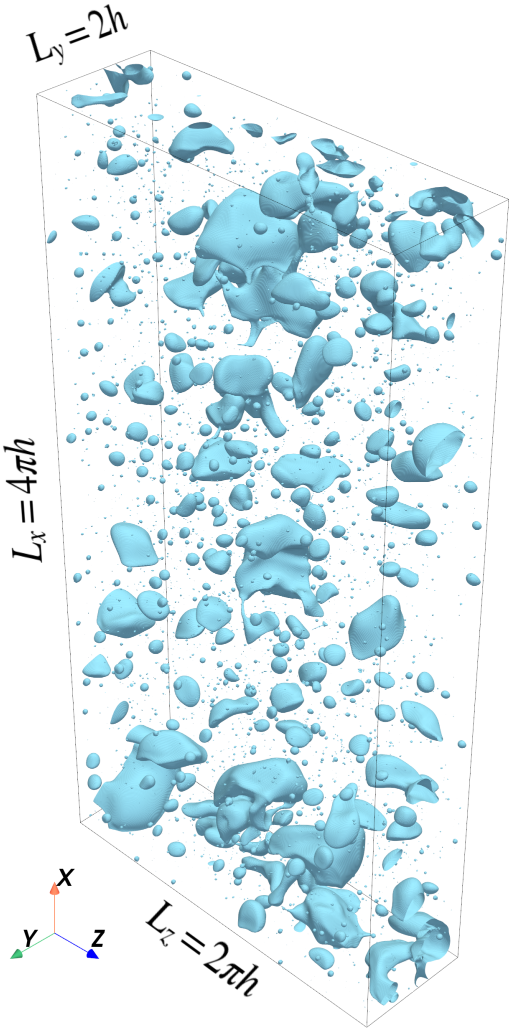

Figure 1: Computational domain and instantaneous rendering of the bubbles at $t^+ \approx 10^3$, after discarding the initial transients, for $We_\tau = 0.7$.

Qualitative features of the bubbly flow

First, as displayed in figure 1, most of the gas volume fraction appears to be encountered in the channel core. This is expected for heterogeneous bubbly flow, as large, deformable bubbles tend to cluster at the center of the channel (Lu & Tryggvason, 2008). This also suggests important bubble-induced agitation at the core of the channel. Moreover, such an effect is probably more pronounced with increasing surface tension (decreasing We_τ) due to the appearance of even larger bubbles. Indeed, as shown by the comparative bar chart in figure 2(a), the highest values of V^+_{bubble} are found within the larger bubble sizes; that is, those having d^+_{eq} (bubble equivalent diameter) larger than d^+_H (Hinze scale, the smallest dimension for a stable fluid particle; Hinze, 1955), and for the highest surface tension case. Here, V^+_{bubble} is the total bubble volume within a range of bubble sizes in the core of the channel; $100 \leq y^+ \leq 200$. Furthermore, as shown in figure 2(b) for $We_\tau = 0.7$ at the channel center, both u'^+ (streamwise velocity fluctuations) and v'^+ (wall-normal velocity fluctuations) are enhanced in the wake of large bubbles. The former mostly in the streamwise direction, whereas the latter both inwards and outwards with respect to the wall-normal direction. It is also noted that the strong, instantaneous velocity structures seem to roughly scale with the

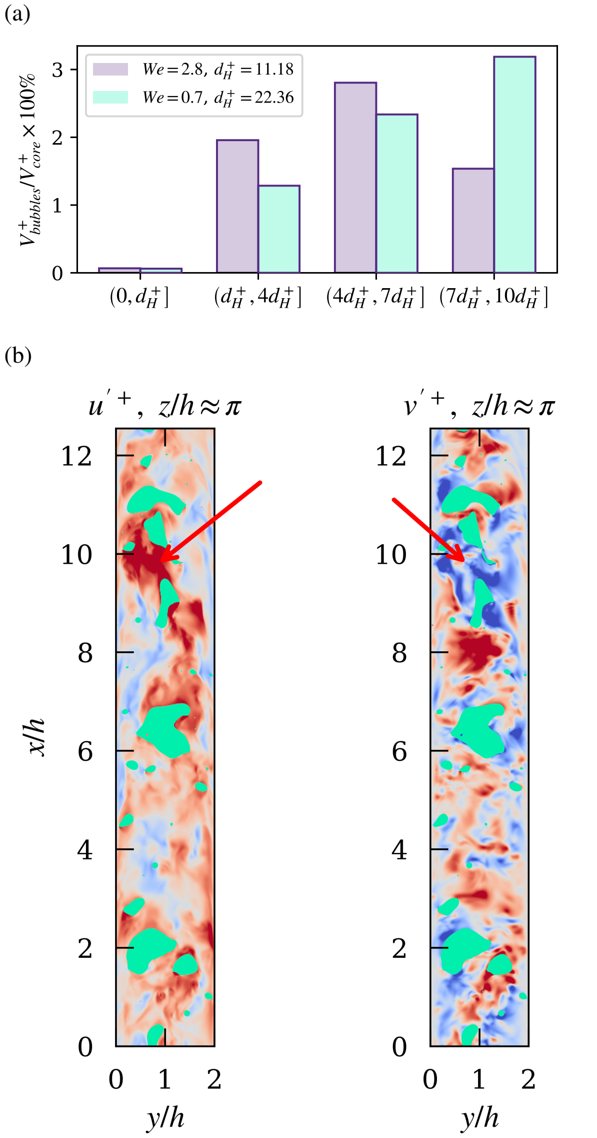

Figure 2: (a) Comparative bar chart for gas volume fraction in the channel core for the different bubbles sizes. (b) Isocontours for streamwise (left) and wall-normal (right) velocity fluctuations in the channel center for $We_\tau = 0.7$. Results are for $t^+ \approx 10^3$, after discarding the initial transients. In (a), $V_{core} = 16\pi^2 h^3/3$. In (b), positive and negative isocontours are respectively identify in red and blue, while bubbles are rendered in green. Also, the red arrows mark some regions of intense fluctuations in the wake of bubbles.

bubble size.

Next, we consider the streamwise and wall-normal velocity spectra at the center of the channel, as well as at $y^+ \approx 12$, closer to the wall. Figure 3 shows the pre-multiplied streamwise and spanwise spectral densities for u'^+ and v'^+, which have been normalized by their respective variances, against the corresponding wavelength. As seen from the figure, there is an overall shift of the spectral content towards smaller scales for the bubble-laden cases when compared to SP. This is particularly conspicuous at the channel center, yet it is also seen to a lesser extent closer to the wall. Interestingly, as shown in panels (a) and (c), there is indeed a correspondence between the scales of the most energetic streamwise velocity structures and the bubble size at the core of the channel. In fact, overlapping at low to moderate wavelengths is recovered for both We_τ cases when normalizing by the respective ${d_H}^+$. See insets. On the other hand, as displayed in panels (b) and (d), the effect of increasing the surface tension (decreasing We_τ) and having larger bubbles on the wall-normal velocity spectra seems negligible. Moreover, as shown in panel (b), very similar streamwise spectral content distributions are seen near the wall and at the channel center, hinting of potentially important interactions between the near-wall structures and those found at the channel core.

States of turbulence in the carrier phase

In order to characterize the states of turbulence in the carrier, we consider the Reynolds stress anisotropy tensor, defined as

$$a_{ij} = \frac{\overline{u}_{ij}}{2k} - \frac{1}{3}\delta_{ij}, \qquad (1)$$

where $\overline{u}_{ij}$, k, and δ_{ij} are the Reynolds stress tensor, turbulent kinetic energy, and Kronecker delta (1 if $i = j$ and 0 otherwise), respectively. Typically, characterization of turbulent states is performed considering tools such as anisotropy invariant maps, which are based on the invariants of a_{ij} (Emory & Iaccarino, 2014). Nevertheless, we can also make a rapid diagnosis by directly considering the components of a_{ij}. For instance, it is well known that in canonical wall-turbulence, very near the wall ($y^+ \approx 10$) most of the turbulent kinetic energy is found in the streamwise velocity component, whereas near the channel center states closer to isotropic conditions are attained (Pope, 2000). Therefore, a_{11} is expected to approach $2/3$ near the wall and 0 at the core of the channel. Figure 4(a) shows that this is indeed so for SP. For the bubble-laden cases, states closer and farther away from isotropic conditions are seen at $y^+ \approx 10$ and $y^+ \approx 150$, respectively. Furthermore, with the exception of the central channel region, the bubble-laden cases are actually closer to isotropic conditions with respect to SP.

The previous observation is further corroborated by means of a barycentric map (BAM; Banerjee *et al.*, 2007) and F (the Lumley's flatness; Lumley, 1979). See figure 4(b) and (c). A BAM is a linear map in the form of an isosceles triangle, delimitating all realizable states of turbulence. The base represents two-component states, that is, when one normal Reynolds stress component is negligible compared to the others, while the right and left hand sides, respectively, identify the axisymmetric expansion (prolate-like) and axisymmetric contraction (oblate-like) states, which converge at the isotropic (*iso*) limit. For further details on the terminology used to identify the states of turbulence, see, e.g., Simonsen & Krogstad (2005). On the other hand, the F parameter is an indicator of proximity to the base of the triangle and to the *iso* limit, taking a value of 1 and 0 for isotropic and two-component turbulence, respectively. Then, as shown in panels (b) and (c), turbulence is indeed more anisotropic for the bubble-laden cases at the channel center. This is expected considering the previous observation about larger bubbles residing in the core of the channel and the consequent appearance of strong bubble-induced fluctuations. Rather surprising, on the other hand, is the fact that this trend is truly only confined to the channel center, and as we move from it, there is actually a higher degree of turbulence anisotropy for SP than for heterogeneous bubbly flow. See profiles that are mostly to the left and above the SP one

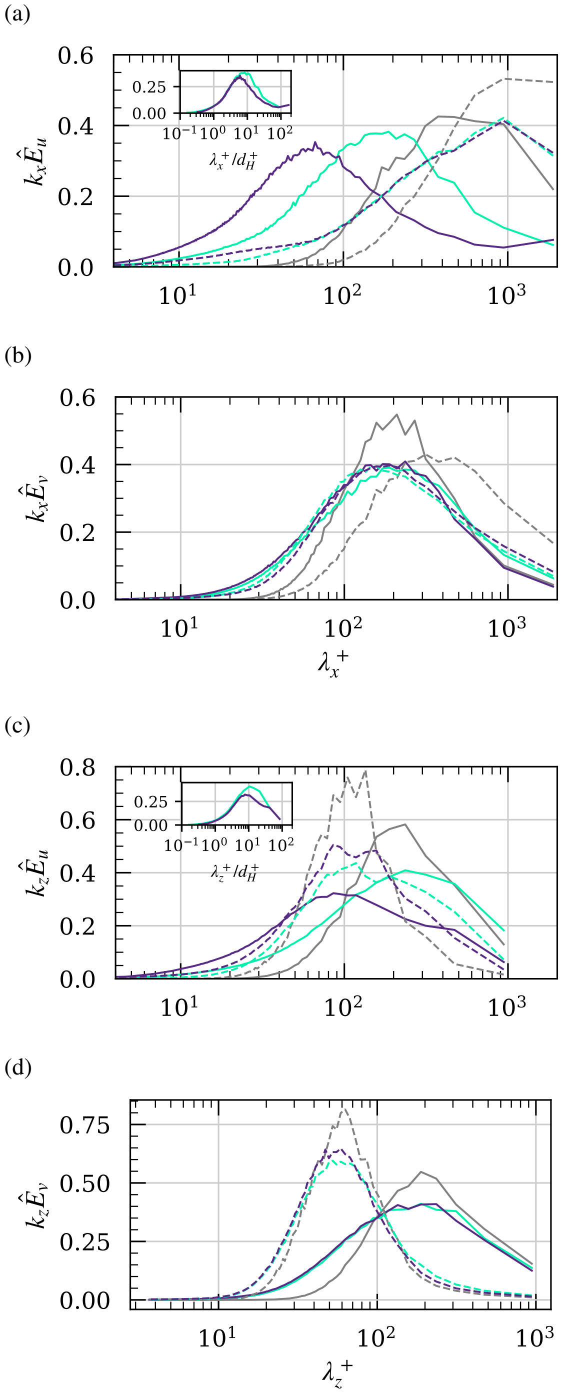

Figure 3: Pre-multiplied, normalized, spectral densities for (a), (c) the streamwise velocity component, $\hat{E}_u$, and (b), (d) the wall-normal velocity components, $\hat{E}_v$. A gray line style is used for SP, whereas cyan and purple line styles are used for the $We_\tau = 0.7$ and 2.8 cases, respectively. Continuous- and dashed-line styles respectively identify profiles at $y^+ = 150$ and $y^+ \approx 12$. Note that, $\lambda_x = 2\pi/k_x$ and $\lambda_z = 2\pi/k_z$ are the wavelengths along the homogeneous directions.

in panels (b) and (c), respectively. It is also interesting to note that this behavior–higher degree of isotropy when compared to SP–is also quite different from the one reported for homogeneous bubbly channel flow. See representative case corresponding to a monodisperse swarm of small bubbles (case labeled as SmMany in Ma *et al.*, 2020) in panel (c), which displays a very anisotropic and approximately constant state of turbulence across a significant portion of the channel.

Sweeps and ejections

Lastly, in light of potentially important inner/outer interactions discussed in the qualitative section and with the purpose of providing a plausible physical explanation for the unexpected changes in turbulence anisotropy for the bubbly-laden cases, we analyze intense momentum transfer events in the wall-bounded flow by means of a quadrant analysis (Wallace, 2016). Figure 5 presents the fractional contribution of sweeps (Q4, high-speed fluid inward) and ejections (Q2, low-speed fluid outward) events to $\overline{u'v'}$ (the Reynolds shear stress). These are the quadrant events that positively contribute to $\overline{u'v'}$, while the others (Q1 and Q3, not shown), simply counterbalance the Q2s and Q4s such that at any y^+, the fractional contribution of the four quadrant events is unitary. Therefore, as seen in the figure, both sweeps and ejections increase for the bubble-laden cases. However, those that significantly deviate from the SP results for most of the channel are the sweeps. It is also noted that there are some differences between the two bubble-laden cases. For $We_\tau = 2.8$, there is still a crossing point where Q2s overcome Q4 events, whereas this is not the case for $We_\tau = 0.7$. In fact, for the former, the sweeps appear to be as important as the ejections for a significant portion of the channel, while for the latter, the sweeps are always the dominant momentum transfer events. In other words, higher momentum in the form of high-speed fluids towards the wall is present for the bubble-laden cases, which may lead to a better redistribution of energy across the channel and explain the observed decrease in anisotropy seen for most of the channel, when compared to SP. In addition, this effect is more pronounced with increasing surface tension (decreasing We_τ), as larger bubbles appear in the core of the channel and there is more bubble-induced agitation; see the qualitative discussion.

CONCLUSIONS

High-fidelity simulations of bubble-laden vertical channel flow were performed. The flow is driven upward by an effective constant pressure gradient, and the deformable bubbles undergo breakage and coalescence. The interface is captured by a VOF method. Three sets of simulations, only differing in their We_τ, were performed to observe the effect of changing the surface tension on the turbulence anisotropy in the carrier. Here, only the results corresponding to $We_\tau = 0.7$ and 2.8 are shown. As a basis for comparison, a SP case with matching Re_τ was also considered.

The main finding is that the turbulence anisotropy in the carrier is actually lower for the multiphase flow cases compared to SP. Only close to the core of the channel where the largest bubbles reside is the opposite true. This is also in striking contrast to results reported for homogeneous bubbly channel flow, where the turbulence anisotropy is actually higher for most of the channel compared to SP (Ma *et al.*, 2020). Such behavior is attributed to an important increase of the momentum transfer events consisting of high-speed fluid towards the wall, which may help to a better redistribution of energy among the different normal Reynolds stress components and across the channel for the considered bubble-laden cases.

Further analyzes, with the aim of clarifying the inner/outer interactions and the transport of turbulent kinetic energy and momentum, may include a full reporting of the velocity spectra and the Reynolds stress budgets.

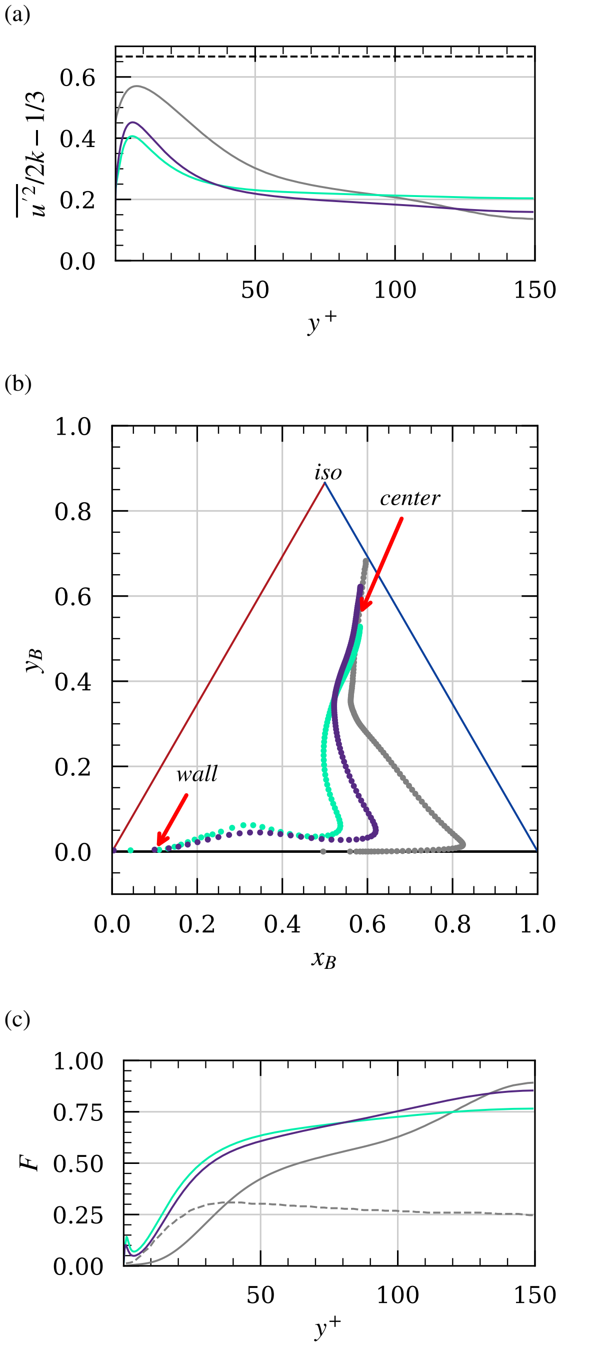

Figure 4: (a) First diagonal component of the Reynolds stress anisotropy tensor, a_{11}, against y^+. (b) Reynolds stress anisotropy in a barycentric map with coordinates x_B, y_B. (c) Lumley's flatness, F, against y^+. Statistics are conditioned to the carrier phase only. A gray line style/marker is used for SP, whereas cyan and purple line styles/markers are used for the $We_\tau = 0.7$ and 2.8 cases, respectively. In (a), a dashed-line style identifies the $2/3$ limit. In (b), red, blue, and black line styles are used to identify the axisymmetric expansion, axisymmetric contraction, and two-component limits, respectively. Also, the isotropic limiting state is labeled as *iso*, while the red arrows (with self-explanatory labels) mark states close to the wall and to the channel center. In (c), a dashed-line style identify results corresponding to homogeneous bubbly flow (case labeled as SmMany in Ma *et al.*, 2020).

ACKNOWLEDGMENTS

Computing resources awarded by EuroHPC (project ID: R0387) and Sigma2 (project ID: NN9646K) are acknowledged. AA and JS also acknowledge financial support by the Research Council of Norway (RCN, grant number: 334652).

REFERENCES

Banerjee, S, Krahl, R., Durst, F. & Zenger, Ch. 2007 Presentation of anisotropy properties of turbulence, invariants versus eigenvalue approaches. *J. Turbul.* **8**, 1–27.

Di Giorgio, S., Pirozzoli, S. & Iafrati, A. 2024 Evaluation of advection schemes and surface tension model for algebraic and geometric VOF multiphase flow solvers. *J. Comput. Phys.* **499**, 112717.

Emory, E. & Iaccarino, G. 2014 Visualizing turbulence anisotropy in the spatial domain with componentality contours. *Center for Turbulence Research, Annual Research Briefs* pp. 123–138.

Garbin, V., Bothe, D., G., Brenn, Casciola, C. M., Colin, C., Marengo, M., Risso, F., Tryggvason, G. & Lohse, D. 2025 Bubbles and bubbly flows. *Int. J. Multiph. Flow* **190**, 105240.

Hinze, J. O. 1955 Fundamentals of the hydrodynamic mechanism of splitting in dispersion processes. *AIChE J.* **1**, 289–295.

Lu, J. & Tryggvason, G. 2008 Effect of bubble deformability in turbulent bubbly upflow in a vertical channel. *Phys. Fluids* **20**, 040701.

Lu, J. & Tryggvason, G. 2018 Direct numerical simulations of multifluid flows in a vertical channel undergoing topology changes. *Phys. Rev. Fluids* **3**, 084401.

Lu, J. & Tryggvason, G. 2019 Multifluid flows in a vertical channel undergoing topology changes: Effect of void fraction. *Phys. Rev. Fluids* **4**, 084301.

Lu, M., Yang, Z. & Deng, B. 2025 Numerical study of turbulent bubbly upflow: Effect of density ratio. *J. Fluid Mech.* **1007**, A63.

Lumley, J. L. 1979 Computational modeling of turbulent flows. *Adv. Appl. Mech.*, vol. 18, pp. 123–176.

Ma, T., Lucas, D., Jakirlić, S. & Fröhlich, J. 2020 Progress in the second-moment closure for bubbly flow based on direct numerical simulation data. *J. Fluid Mech.* **883**, A9.

Pirozzoli, S. & Orlandi, P. 2021 Natural grid stretching for DNS of wall-bounded flows. *J. Comput. Phys* **439**, 110408.

Pope, S. B. 2000 *Turbulent Flows*. CUP.

Procacci, D., Arosemena, A. A., Di Giorgio, S. & J., Solsvik 2026 Turbulence anisotropy modulation in bubble-laden channel flow: A numerical study. *Int. J. Multiph. Flow* **195**, 10550.

Risso, F. 2018 Agitation, mixing, and transfers induced by bubbles. *Annu. Rev. Fluid Mech.* **50**, 25–48.

Rossi, D., Di Giorgio, S. & Pirozzoli, S. 2025 Comparative analysis of volume of fluid and phase-field methods for numerical simulations of two-phase flows. *Int. J. Multiph. Flow* **189**, 105245.

Simonsen, A.J. & Krogstad, P.-Å. 2005 Turbulent stress invariant analysis: Clarification of existing terminology. *Phys. Fluids* **17**, 088103.

Wallace, J. M. 2016 Quadrant analysis in turbulence research: History and evolution. *Annu. Rev. Fluid Mech.* **48**, 131–158.

Weymouth, G.D. & Yue, D. K. P. 2010 Conservative volume-of-fluid method for free-surface simulations on Cartesian-grids. *J. Comput. Phys.* **229**, 2853–2865.

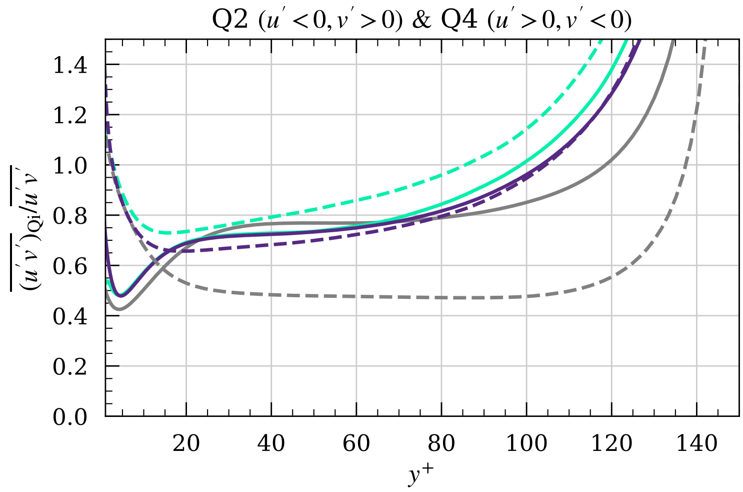

Figure 5: Fractional contribution of ejections (Q2) and sweeps (Q4) to the shear Reynolds stress, $\overline{(u'v')}_{Qi}/\overline{u'v'}$, against y^+. A gray line style is used for SP, whereas cyan and purple line styles are used for the $We_\tau = 0.7$ and 2.8 cases, respectively. Continuous- and dashed-line styles respectively identify the fractional contributions of the Q2 and Q4 events. Statistics are conditioned to the carrier phase only.